



# In-depth insight into the mechanism on photocatalytic synergistic removal of antibiotics and Cr (VI): The decisive effect of antibiotic molecular structure

Qiang Zhang<sup>1</sup>, Juan Chen<sup>1</sup>, Xin Gao, Huinan Che, Peifang Wang<sup>\*</sup>, Yanhui Ao<sup>\*</sup>

Key Laboratory of Integrated Regulation and Resource Development on Shallow Lakes of Ministry of Education, College of Environment, Hohai University, No. 1, Xikang Road, Nanjing 210098, China

## ARTICLE INFO

### Keywords:

Synergistic effect  
Antibiotics  
Electron-donating ability  
Cr (VI)  
DFT calculation

## ABSTRACT

Antibiotics and heavy metal contaminants often coexist in wastewater but their simultaneous/synergistic removal remains a great challenge. Herein, a synergistic effect on the photocatalytic removal of antibiotics and hexavalent chromium (Cr (VI)) is realized using ultra-thin g-C<sub>3</sub>N<sub>4</sub>. The mechanism of synergistic effect is studied deeply at molecular level through experiments and theoretical calculation. Antibiotics molecules are first adsorbed on the surface of g-C<sub>3</sub>N<sub>4</sub> by  $\pi$ - $\pi$  interactions, and subsequently act as electron donors (hole sacrificial agents) to accelerate the separation of photo-generated electron-hole pairs and allow more electrons/holes to participate in the redox reaction. Another crucial finding is that there is a linear relationship between the electron-donating capacity and the synergistic efficiency. Detailly, the contaminant molecules with greater electron-donating capacity are more favorable to the improvement of synergistic efficiency. Our work systematically analyzes the mechanism of synergistic effect on contaminants removal and proposes reasonable methods to enhance the synergistic efficiency.

## 1. Introduction

Generally, the wastewater from industry and life contains a variety of contaminants such as organic pollutants, heavy metal pollutants, biological pollutants, etc. [1–4]. Among these pollutants, antibiotics have become a research hotspot owing to their serious harm to organisms (health threats and bacterial resistance) [5–8]. Enoxacin (ENO), as a typical fluoroquinolone antibiotic, has been widely used in the treatment of bacterial infections because of its potent bactericidal properties. ENO released into the water environment through animal metabolism can cause serious harm to aquatic animals and plants [9]. Unfortunately, the stable piperazine ring structure of ENO makes it difficult to be degraded naturally. In addition, Cr (VI) usually coexists with antibiotics in wastewater which is another focus of concern [10–12]. It is a pity that the removal of antibiotics and Cr (VI) through traditional methods is very inefficient because of their relative stability and non-biodegradability [13–15]. Besides, the simultaneous or synergistic removal of antibiotics and Cr (VI) is still a great challenge.

Photocatalytic technology provides a promising strategy for

simultaneous or synergistic removal of antibiotics and Cr (VI) [16,17]. In the photocatalytic process, the photocatalyst absorbs photons and generates photo-generated electrons and holes [18–21]. After that, antibiotic pollutants in wastewater could be eliminated by photocatalytic oxidation reaction and produce H<sub>2</sub>O, CO<sub>2</sub>, or other small molecules [22, 23]. On the other hand, highly toxic Cr (VI) could be reduced to low-toxicity trivalent chromium (Cr (III)) through photocatalytic reduction reaction [24–26]. At last, the simultaneous removal of antibiotics and Cr (VI) is achieved. Previous studies have demonstrated the reliability of simultaneous or synergistic removal of antibiotic pollutants and Cr (VI). For example, Chen et al. prepared Ag/AgBr/BiVO<sub>4</sub> ternary composites by hydrothermal and photoreduction methods and realized the simultaneous removal of ciprofloxacin (CIP) and Cr (VI) [27]. Huang and co-workers reported p-n heterojunction rGO/Cu<sub>2</sub>O/BiVO<sub>4</sub> composites, which ensured the effective removal of sulfamethoxazole (SMZ) and Cr (VI) in the coexistence system [28]. Other photocatalysts such as biochar-coupled g-C<sub>3</sub>N<sub>4</sub> nanosheets (BPCMSs/g-C<sub>3</sub>N<sub>4</sub> NSs) composites [29], MIL-53 (Fe)/CQDs/MNPs [30], etc. also have excellent photocatalytic performance in removing organic contaminants and Cr (VI)

<sup>\*</sup> Corresponding authors.

E-mail addresses: [pfwang2005@hhu.edu.cn](mailto:pfwang2005@hhu.edu.cn) (P. Wang), [andyao@hhu.edu.cn](mailto:andyao@hhu.edu.cn) (Y. Ao).

<sup>1</sup> The two authors contribute equally to the work.

simultaneously. The above works have achieved excellent results in the simultaneous or synergistic removal of antibiotic pollutants and Cr (VI). The fly in the ointment is that these works have only focused on the synthesis of photocatalysts and the efficiency of synergistic removal [31], while the mechanism of synergistic removal of antibiotic pollutants and Cr (VI) is less studied. Understanding and revealing the mechanism of synergistic removal at the molecular level is essential for the development of efficient photocatalysts.

In response to the above problems, a simple and efficient photocatalyst (graphitic carbon nitride ( $g\text{-C}_3\text{N}_4$ )), was used to study the mechanism of synergistic removal of antibiotic pollutants and Cr (VI).  $g\text{-C}_3\text{N}_4$ , a typical polymer semiconductor material, possesses a favorable redox ability on account of the unique structure and the suitable bandgap [32,33]. Unlike the photocatalysts reported above, the synthetic methods of  $g\text{-C}_3\text{N}_4$  are easy and low-cost. More importantly, it is non-toxic and harmless to aquatic animals and plants, thus is favorable for practical application [31,34]. Based on the above advantages, it is a wonderful choice to eliminate the contaminants in wastewater using  $g\text{-C}_3\text{N}_4$  [35,36].

Herein,  $g\text{-C}_3\text{N}_4$  was synthesized by traditional methods based on our previous work [37]. Besides, common antibiotic pollutants (ENO) and Cr (VI) are chosen to investigate their removal mechanisms in the single and coexistence systems. The experimental results show that there is a synergistic removal effect in the coexistence systems. Afterward, a clearer and more detailed mechanism of synergy effect is proposed by the combination of experiments and DFT calculation. Besides, the influence of the molecular structure of pollutants (electron-donating ability), pollutant concentration and pH value on the synergistic efficiency is tested and analyzed. At last, the feasible degradation pathways of ENO are put forward by the combination DFT theoretical calculation and LC-MS test.

## 2. Experimental section

### 2.1. Synthesis of photocatalysts

Scheme S1 displays the detailed preparation steps for pristine  $g\text{-C}_3\text{N}_4$  and the modified  $g\text{-C}_3\text{N}_4$ . Pristine  $g\text{-C}_3\text{N}_4$  was manufactured by a simple thermal polymerization method of dicyandiamide. Detailly, dicyandiamide (10 g) was placed into a 50 mL porcelain crucible with a cover. Afterward, the crucible was calcined in a muffle furnace at 550 °C for 4 h with a ramping rate of 10 °C  $\text{min}^{-1}$  and then cooling to room temperature naturally. The obtained yellow samples were denominated as CN. The modified  $g\text{-C}_3\text{N}_4$  was synthesized by the two-step calcination method. In detail, the prepared CN samples (1.5 g) were put into a porcelain boat and calcined in a muffle furnace at 500 °C for 4 h using a ramping rate of 5 °C  $\text{min}^{-1}$ . The generated faint-yellow samples were denominated as CNN.

### 2.2. Photocatalytic removal experiments

Photocatalytic removal experiments of pollutants in wastewater were simply simulated by enoxacin (ENO) degradation and Cr (VI) reduction under visible light. A 300 W Xe lamp was employed as the light source ( $\lambda > 420 \text{ nm}$ ). Typically, photocatalyst (25 mg) was put into the reaction solution (50 mL) and then sonicated for 5 min to fully disperse the catalyst. Subsequently, the mixed solution was stirred for 30 min in the dark to reach an adsorption-desorption balance. The different pH value of the initial reaction solution was adjusted by 0.1 mol  $\text{L}^{-1}$  HCl and 0.1 mol  $\text{L}^{-1}$  NaOH solution. During the reaction process, the temperature of the reaction liquid was maintained at 25 °C through a circulating water pump. About 2 mL suspension was extracted by 2.5 mL plastic injectors at 0, 2, 4, 6, 8, 10 min, and then the resulting solution was filtrated through a 0.22  $\mu\text{m}$  membrane filter to remove the photocatalysts particles.

The concentration of ENO was detected via high-performance liquid

chromatography (HPLC, Waters e2695), equipped with a C18 column. The chromatography operating conditions of ENO are as follows: the column temperature is 30 °C, the mobile phase is acetonitrile, and 0.1% methanoic acid (volume ratio is 35%: 65%) at a flow rate of 1.0 mL  $\text{min}^{-1}$  and injection volume is 20  $\mu\text{L}$ , the variable wavelength detector was set at 269 nm. The concentration of Cr (VI) was measured by the 1, 5-diphenylcarbazide (DPC) colorimetric method. In detail, 1 mL filtrated solution was added to 9 mL  $\text{H}_2\text{SO}_4$  solution (0.2 mol  $\text{L}^{-1}$ ). Then, add 200  $\mu\text{L}$  1, 5-diphenylcarbazide solution (2.5 g  $\text{L}^{-1}$ ) to the mixed solution. The resulting purple solution was tested at 540 nm on a UV-vis spectrometer (UV-3600, Japan).

### 2.3. Characterization of photocatalysts

X-ray diffraction (XRD) patterns of the prepared catalysts were collected to observe their crystal structure. Fourier transform infrared (FTIR) spectroscopy explored the chemical structure of all catalysts. X-ray photoelectron spectroscopy (XPS, ThermoFisher, Nexsa) was utilized to detect the chemical composition and surface elements of all samples. The morphology and microstructure of catalysts were conducted by transmission electron microscope (TEM). The UV-vis spectra of all catalysts were determined using a UV-vis spectrometer (UV-3600, Japan). Additionally, to gain the specific surface areas of samples, the Brunauer-Emmett-Teller (BET) method was utilized on micromeritics (ASAP 2460 3.01). The electrochemical workstation (CHI660D) was conducted to record the electrochemical properties of the produced samples. The specific operation steps refer to the previous research [38]. The photoluminescence spectroscopy (PL) with 370 nm excitation wavelength was measured on fluorescence spectrometer (F-7000, Hitachi, Japan). The Electron spin resonance (ESR) was performed in Bruker ESR JESFA200 spectrometer.

### 2.4. Theoretical calculation

Density functional theory (DFT) calculations were conducted using Gaussian 16, Revision C.01 program package [39].  $\pi\text{-}\pi$  interactions and frontier orbit distribution (HOMO, LUMO) of ENO/ $g\text{-C}_3\text{N}_4$  system are obtained by optimizing its molecular structure with B3LYP-D3BJ theoretical method [40] on standard 6-31 G(d) [41,42] basis set. The ionization potential of different pollutants is calculated using the M06-2X method on a standard 6-31G(d) [41,42] basis set. Noteworthy, the Solvation Model Based on Density (SMD) [43] took the Solvent effect of  $\text{H}_2\text{O}$  into account. To predict the reactive sites of ENO, the Fukui function ( $f^+$ ,  $f^-$ ,  $f^0$ ), condensed dual descriptor (CDD) (Note S2) and Hirshfeld charges of ENO molecules were produced by Multiwfn 3.8 [44]. All images were drawn by VMD (1.9.3 version) procedures.

## 3. Results and discussion

### 3.1. The removal of ENO and Cr (VI) in the single and coexistence systems

To demonstrate that the removal reaction of ENO and Cr (VI) is indeed driven by the photocatalytic process, the removal experiments of ENO and Cr (VI) are employed in the single and coexistence system without catalysts. As illustrated in Fig. S1, ENO and Cr (VI) cannot be removed in the absence of catalysts, which implies that ENO and Cr (VI) are relatively stable and do not react with each other under visible light irradiation. Dark reaction experiments are performed for 30 min to ensure that the mixture reached adsorption-desorption equilibrium. As shown in Fig. S2, the mixed solution reaches adsorption-desorption equilibrium within 30 min in the single and coexistence systems. Moreover, the adsorption performance of CNN is relatively higher than that of CN, which is conducive to the removal reaction of pollutants. Afterwards, the photocatalytic degradation results of ENO in the single and coexistence systems are displayed in Fig. 1a. In the single system, it

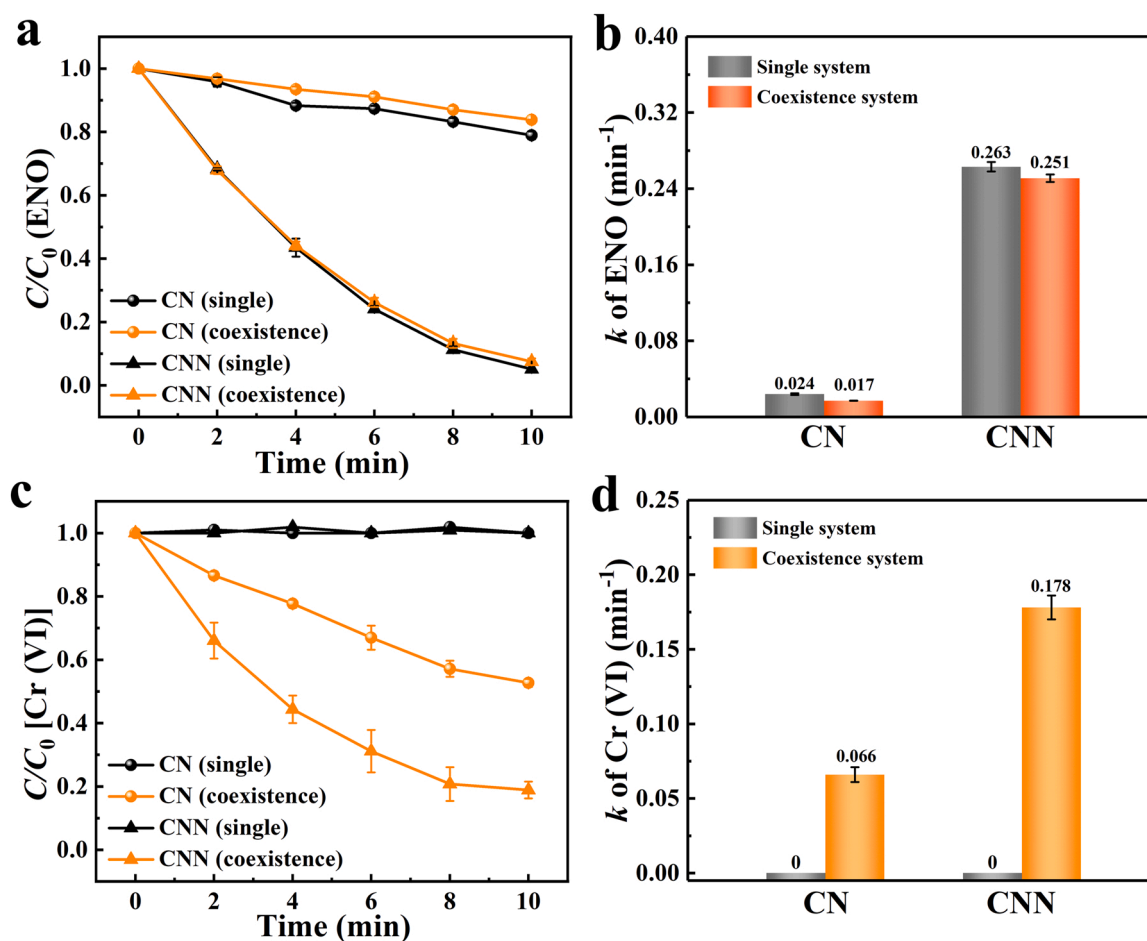
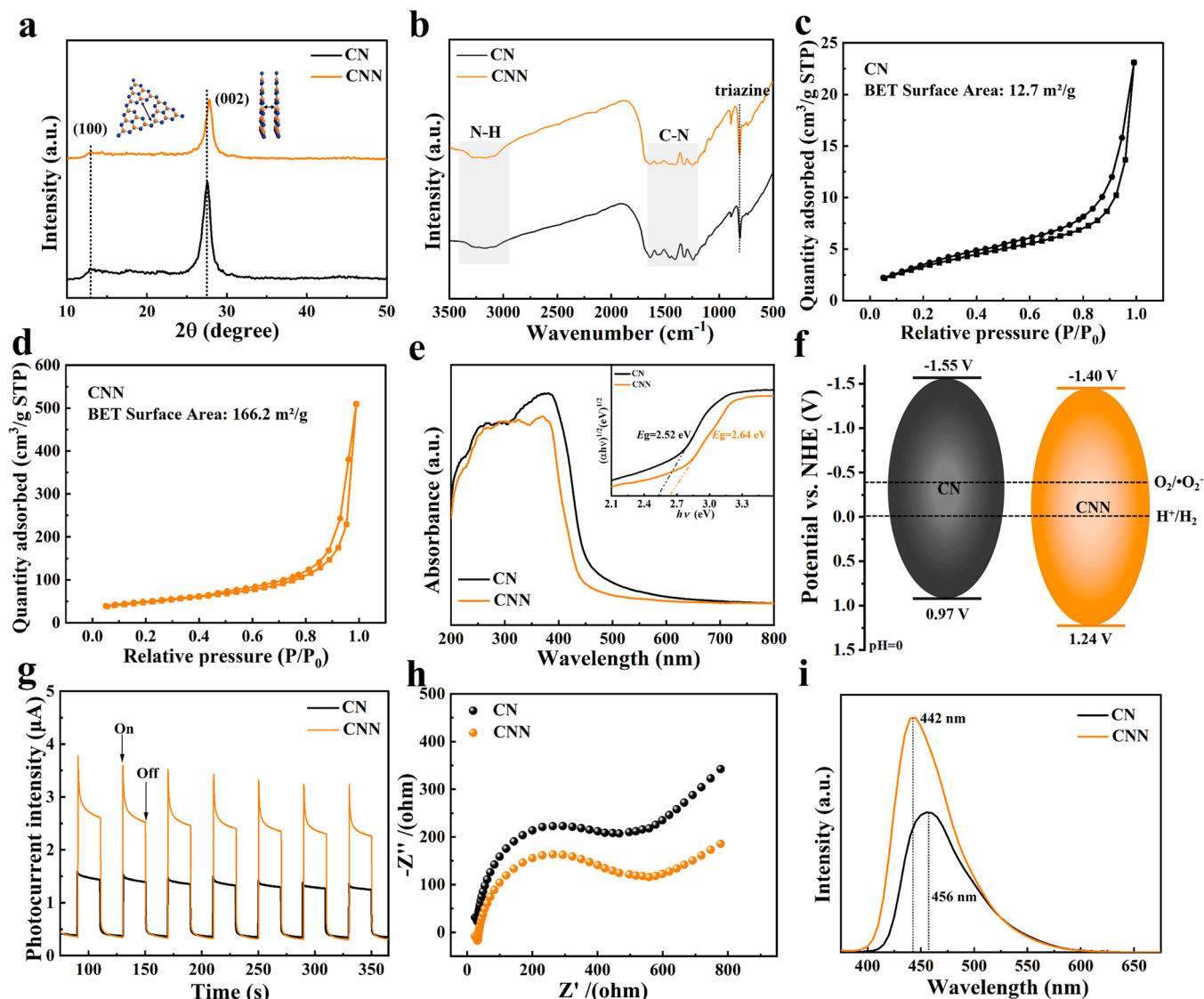


Fig. 1. (a) The degradation experiment and (b) the  $k$  value of ENO by CN and CNN in the single and coexistence systems. (c) The reduction experiment and (d) the  $k$  value of Cr (VI) by CN and CNN in the single and coexistence systems. [ $C_{\text{ENO}}$ ] = 20 mg/L, [ $C_{\text{Cr (VI)}}$ ] = 2 mg L<sup>-1</sup>].

is obvious that CN possesses a sluggish photocatalytic degradation activity and the degradation rate of ENO within 10 min is approximately 21.1%. However, the degradation efficiency of ENO by CNN is significantly better than that of CN, which reaches up to 92.6% within 10 min. The first-order kinetic constants ( $k$ ) of the ENO degradation also prove that CNN has a higher  $k$  value (0.26 min<sup>-1</sup>), which is approximately 11.3 times higher than CN (0.024 min<sup>-1</sup>) (Fig. 1b). In the coexistence system, whether using CN or CNN, the degradation efficiency of ENO does not change much compared to the single system. Among them, the degradation rate of ENO by CNN still maintains a high level (Fig. 1a-b). Subsequently, the reduction experiments of Cr (VI) by CN and CNN in the single and coexistence systems are further measured. As depicted in Fig. 1c, the concentration of Cr (VI) has barely changed even with the presence of CN or CNN in the single system, indicating the poor reduction activity of CN and CNN for Cr (VI). Whereas, the reduction efficiency of Cr (VI) by CN and CNN is significantly improved in the coexistence system. Especially, the reduction rate of Cr (VI) by CNN is as high as 81.1% within 10 min. From Fig. 1d, the  $k$  of Cr (VI) removal by CN increased from 0 to 0.066 min<sup>-1</sup> and increased from 0 to 0.18 min<sup>-1</sup> by CNN in the coexistence system. Similarly, CNN has a higher removal efficiency for Cr (VI), over 2.7 times than that of CN. Based on the above results, it is found that the photocatalytic redox activity of CNN is significantly higher than that of CN whether in the single or coexistence system. An even more crucial discovery is that the presence of ENO can substantially increase the reduction rate of Cr (VI) by both CN and CNN, and the degradation efficiency of ENO is still preserved at a high level. Therefore, a synergistic effect is achieved in the removal of ENO and of Cr (VI).

### 3.2. The mechanism of enhanced photocatalytic performs for CNN

To unveil the reasons for the enhanced degradation performance of CNN, the changes in the crystal structure and surface functional groups of catalysts are firstly analyzed using XRD, FTIR and XPS. From Fig. 2a, (100) and (002) characteristic peaks are exhibited in the XRD spectra, which correspond to the in-plane structural packing of tri-s-triazine units and the interlayer stacking of conjugated aromatic systems [1,45,46], respectively. Interestingly, the diffraction peak intensity of CNN is weaker than that of CN and the peak position of CNN shifted to the right slightly, which is attributed to the narrowed stacking distance between g-C<sub>3</sub>N<sub>4</sub> layers [18,47]. The FTIR spectra of CN and CNN in Fig. 2b present similar characteristic vibration modes. Detailly, the main absorption bands at around 810 cm<sup>-1</sup>, 1200–1700 cm<sup>-1</sup> and 3000–3400 cm<sup>-1</sup> are correlated to the triazine ring bending vibration, C-N stretching vibrations and N-H stretching vibrations, respectively [3,48,49]. XPS was carried out to further examine the surface compositions and surface states of prepared samples. As displayed in Fig. S4a, all characteristic peaks of constituent elements in the corresponding catalysts can be clearly observed including C, N and O. In high resolution C 1 s spectra (Fig. S4b), there are three peaks at 284.8 eV, 286.6 eV and 288.2 eV severally assigned to the existence of C-C/C=C bond, C-NHx and sp<sup>2</sup> N=C-N bonds [50], respectively. Interestingly, the intensity of C-C/C=C bond for CNN is distinctly weaker than that of CN, which indicates the loss of C species. The N 1 s spectra (Fig. S4c) exhibited four signals located at 398.7 eV, 400.2 eV and 401.4 eV, representing C=N-C, C-NHx and N-(C)<sub>3</sub>, respectively [51]. From Fig. S4d, the C/N ratio is from 0.89 for CN to 0.75 for CNN, further means that the small



**Fig. 2.** (a) XRD spectra and (b) FTIR spectra of CN and CNN. The BET surface area of (c) CN and (d) CNN. (e) The UV-vis diffuse reflectance spectra (DRS) of CN and CNN. (f) The electronic band structure of CN and CNN. (g) Photocurrent intensity, (h) EIS and (i) PL spectra of CN and CNN.

loss of C species from CN. However, it is obvious that both C 1 s and N 1 s peaks of the prepared samples are not significantly shifted, indicating that the surface chemical compositions of CN and CNN are structurally, which is consistent with the FTIR analysis. According to the above characterizations, it can be judged that the crystal structure and functional groups of CNN have no obvious change compared to that of CN.

The morphology of CN and CNN is researched by TEM (Fig. S5). Obviously, the thickness of CNN is distinctly thinner than that of CN, which is consistent with previous reports [52]. The specific surface area analysis based on BET (Fig. 2c-d) shows that CNN possesses a larger specific surface area than that of CN. Generally, the thinner structure and larger specific surface area can provide more adsorption and reaction sites for pollutants. As depicted in the adsorption experiments of CN and CNN (Fig. S2), the adsorption performance of CNN is relatively higher than that of CN in both the single and coexistence system. Theoretically, the adsorption capacity of pollutants on the catalyst is a key factor in determining degradation efficiency. Therefore, one reason for the enhanced degradation activity of CNN is that CNN possesses a thinner structure and larger specific surface area compared to CN. That is to say, CNN can provide more adsorption and reaction sites for ENO, which is conducive to the degradation of ENO.

The UV-vis diffuse reflectance spectra (DRS) and Mott-Schottky plot are utilized to record the changes in the electronic band structure of samples. As seen in Fig. 2e, compared to that of CN, the absorption edge of CNN is slightly blue shift and the light absorption ability is marginally decreased. The calculated bandgaps (Note S3) of CN and CNN by the absorption edge are 2.52 eV and 2.64 eV [38,53], respectively. From Fig. S6, the flat band potential determined by the Mott-Schottky plot is  $-1.75$  V and  $-1.60$  V (vs. Ag/AgCl) for CN and CNN, respectively, which are converted into  $-1.55$  V and  $-1.40$  V (vs. NHE) [35]. Combining the calculated bandgap and CB position of catalysts, the valance band (VB) position can be deduced. As shown in Fig. 2f, the VB position of CNN is lower than that of CN, clarifying that the oxidation ability of  $h^+$  in CNN is stronger. In other words, CNN is more conducive to the oxidation of ENO with respect to CN. Additionally, photocurrent response experiments show that the photocurrent density of CNN is 2-folds than that of CN (Fig. 2g), indicating the faster separation and transfer rate of photogenerated charge carrier in CNN. The results of EIS measurements are shown in Fig. 2h, and CNN owns the smaller arc radius than that of CN, further indicating that the carrier is subject to less resistance during transport. Interestingly, PL spectra (Fig. 2i) shows that CNN has a higher peak strength compared to CNN, which is attributed to



the quantum limiting effect of g-C<sub>3</sub>N<sub>4</sub> nanosheets [18]. Meanwhile, the peak of CNN is also blue shifted, which corresponds to the results of DRS results. Overall, the photocatalytic activity of CNN is significantly higher than that of CN since the combined action of the larger specific surface area, higher oxidation capacity and faster carrier separation efficiency.

### 3.3. The mechanism of synergistic effect in the coexistence system

In order to have a deep understanding of the mechanism of the synergistic effect of ENO and Cr (VI) in the coexistence system, the free radical quenching experiments are carried out to determine the active species. The introduction of triethanolamine (TEOA, holes scavenger), isopropanol (IPA, the scavenger of hydroxyl radicals), and argon (Ar, the scavenger of superoxide radicals) are served as quenchers in the single system of ENO solution. As shown in Fig. 3a, the degradation rate of ENO is significantly reduced after injecting TEOA, clarifying that holes ( $h^+$ ) play a major role in the degradation process of ENO. When Ar is introduced during the reaction process, the degradation efficiency of ENO is slightly inhibited, implying that the degradation process of ENO also has the contribution of superoxide radicals ( $\cdot O_2^-$ ). Hydroxyl radicals ( $\cdot OH$ ) makes little contribution to the degradation of ENO owing to the degradation rate has no change after injecting IPA. Moreover, the  $k$  of ENO and the active species contribution rate in Fig. 3b also prove the key role of  $h^+$  and  $\cdot O_2^-$  in the degradation of ENO. ESR spectra was performed to detect the presence and content of active species under light irradiation. As displayed in Fig. S7, CNN sample contains more  $h^+$ ,  $\cdot O_2^-$  and  $\cdot OH$  content compared to CN, which is consistent with the higher photocatalytic performance of CNN. For the removal of Cr (VI), previous reports have already demonstrated that the photocatalytic reduction of

Cr (VI) is the contribution of photoinduced electrons ( $e^-$ ) [54]. Undoubtedly, the reduction efficiency of Cr (VI) is hindered in the oxygen ( $O_2$ ) atmosphere due to  $e^-$  can interact with  $O_2$  to produce  $\cdot O_2^-$ , as indicated in Fig. 3c. Meanwhile, when NaBrO<sub>3</sub> ( $e^-$  scavenger) is added to the coexistence system, the removal rate of Cr (VI) is distinctly reduced, further demonstrating the key role of  $e^-$  in the photoreduction reaction of Cr (VI). However, the reduction reaction of Cr (VI) ions is also a process of capturing  $e^-$ , so the addition of  $O_2$  and NaBrO<sub>3</sub> cannot completely suppress the removal of Cr (VI). Interestingly, the reduction rate of Cr (VI) is remarkably increased when TEOA and MeOH are added to the single system of Cr (VI) (Fig. 3d). As we know, TEOA and MeOH could act as  $h^+$  scavenger or electron donors in the photocatalytic process [55], which consume lots of photo-generated  $h^+$  to make more photo-generated  $e^-$  participate in the photocatalytic reduction reaction. Accordingly, the reduction efficiency of Cr (VI) is significantly promoted in the presence of TEOA or MeOH compared to the blank experiment. Among them, the addition of TEOA has a better effect on the reduction of Cr (VI) than MeOH, which is attributed to the better  $h^+$  removal efficiency of TEOA [55]. Inspired by this, we speculate that ENO can also act as an electron donor or  $h^+$  scavenger to enable more photo-generated  $e^-$  on the surface of g-C<sub>3</sub>N<sub>4</sub> to participate in the reduction of Cr (VI), just like the role of TEOA and MeOH. To preliminarily prove this conjecture, the influence of different pollutants on the photocurrent intensity is investigated. From Fig. S8, it is clear that the photocurrent intensity of CNN in the presence of ENO is stronger than the absence of ENO, indicating the faster charge transfer and separation efficiency. When Cr (VI) is present in the solution, there is no significant change in the photocurrent intensity of CNN compared to that of CNN. This phenomenon indicates that Cr (VI) cannot be removed by CNN in the presence of Cr

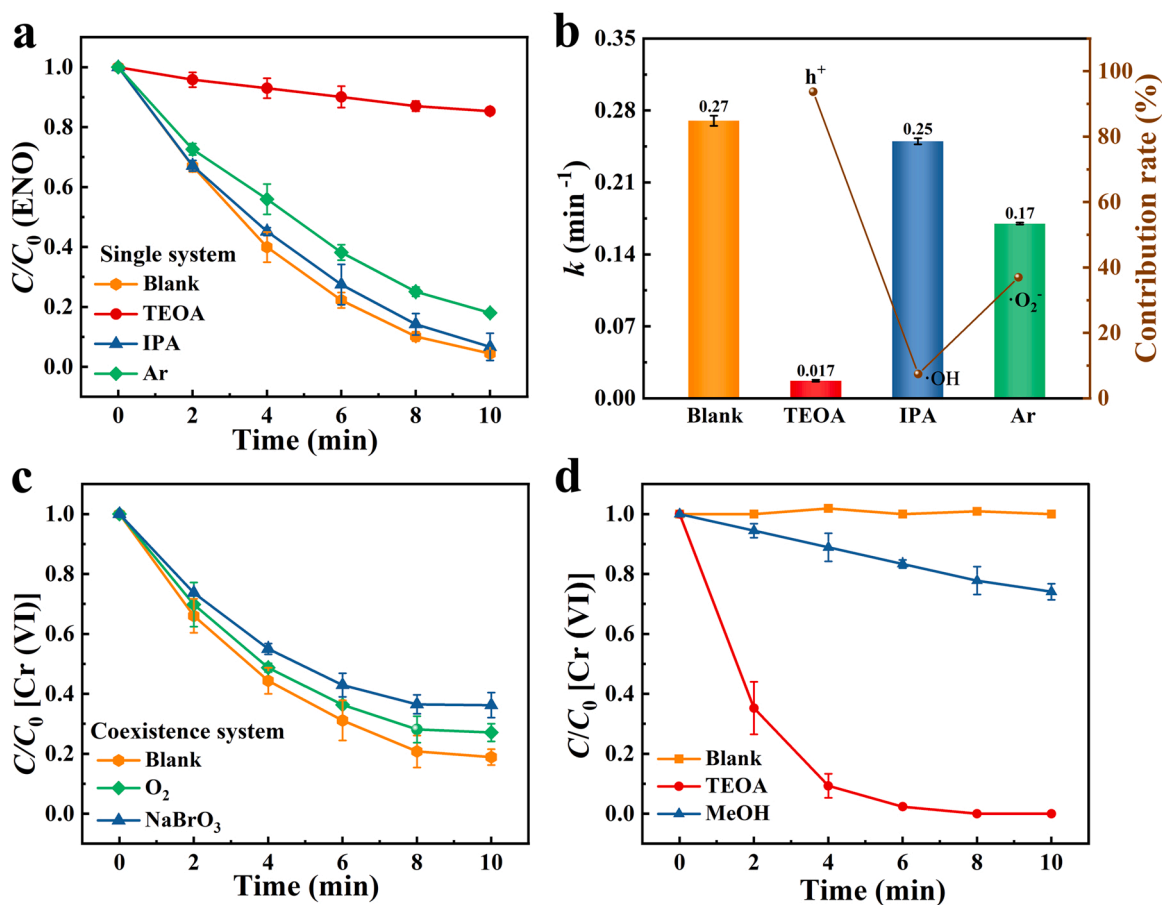


**Fig. 3.** (a) The free radical quenching experiments of CNN on the degradation of ENO in the single system. (b) The first-order reaction kinetic constants ( $k$ ) and the active species contribution rate of CNN on the degradation of ENO in the single system. (c) The quenching experiments of CNN on the reduction of Cr (VI) in the coexistence system. (d) The effect of TEOA and MeOH on the reduction of Cr (VI) in the single system. [ $M_{(TEOA)} = M_{(MeOH)} = 0.01 \text{ mol L}^{-1}$ ].

(VI) alone. However, the photocurrent intensity of CNN in the coexistence system is distinctly decreased, indicating that the removal of Cr (VI) is the function of  $e^-$  and the removal reaction expends large amounts of  $e^-$ .

The theoretical calculation based on DFT is performed to further demonstrate the role of ENO as electron donors. Here, we firstly studied the interface interaction and molecular orbital distribution between ENO and g-C<sub>3</sub>N<sub>4</sub>. The optimized structure of the ENO/g-C<sub>3</sub>N<sub>4</sub> system is displayed in Fig. S9. Based on the  $\pi$ -conjugated structure of ENO and g-C<sub>3</sub>N<sub>4</sub>, the  $\pi$ - $\pi$  interactions between ENO and g-C<sub>3</sub>N<sub>4</sub> are described by the reduced density gradient (RDG) method (Fig. 4a) [56]. The  $\pi$ - $\pi$  interactions have an important role in the adsorption and electron transfer between ENO and g-C<sub>3</sub>N<sub>4</sub>, as previously reported [57,58]. Further, by comparing the results from the distribution of frontier molecular orbital (Fig. 4b-c), it is found that HOMO is mainly distributed in ENO and LUMO is distributed on g-C<sub>3</sub>N<sub>4</sub>. Theoretically, the electrons on HOMO tend to transfer to LUMO, which is ascribed to HOMO as the nature of electron donors and LUMO as the nature of electron acceptors [59]. Therefore, in the photocatalytic removal of pollutants, ENO is first adsorbed on the surface of g-C<sub>3</sub>N<sub>4</sub> by  $\pi$ - $\pi$  interactions. On the one hand, ENO act as electron donors and consumes large number of  $h^+$  on the surface of g-C<sub>3</sub>N<sub>4</sub>, allowing more  $e^-$  on the surface of g-C<sub>3</sub>N<sub>4</sub> to participate in the photocatalytic reduction of Cr (VI). On the other hand, the reduction of Cr (VI) spend much  $e^-$  on the surface of g-C<sub>3</sub>N<sub>4</sub> and further accelerate the separation of photo-generated  $e^-$  and  $h^+$ , which ensure more  $h^+$  join in the degradation of ENO. Accordingly, the degradation efficiency of ENO still maintains a high level even with the decrease of the content of  $\cdot O_2$  (more  $e^-$  is consumed by Cr (VI)).

For the single system of Cr (VI), both CN and CNN have a very poor reduction efficiency. The main reason for this low efficiency is that the weak photocatalytic activity of g-C<sub>3</sub>N<sub>4</sub> does not have sufficient driving

force to achieve the rapid reduction of Cr (VI) in a short time without electron donor. Moreover, as shown in Fig. S10, the surface potential of CNN is negative. And, the main forms of Cr (VI) are  $HCrO_4^-$  and  $CrO_4^{2-}$  in neutral solution [54]. As we know, the electrostatic repulsion would be produced between catalysts and Cr (VI) ions since the same charge of them, which suppresses the adsorption process of Cr (VI). It results in a particularly poor photocatalytic reduction rate of Cr (VI) by CNN. However, in the coexistence system, the presence of the electron donors (ENO) greatly improves the charge separation of g-C<sub>3</sub>N<sub>4</sub>, providing a strong driving force for Cr (VI) reduction. Therefore, the adverse effect of electrostatic repulsion between catalysts and Cr (VI) is relatively small.

#### 3.4. The effect of molecular structure of contaminants, concentration of ENO and pH on the synergistic reduction of Cr (VI)

The other two contaminants, bisphenol A (BPA) and sulfamethoxazole (SMZ), as common water pollutants, are used to explore the effect of electron-donating capacity of pollutants on the synergistic reduction of Cr (VI). Similarly, the dark reaction experiments are performed for 30 min to ensure that the pollutants reached adsorption-desorption equilibrium (Fig. S11). As depicted in Fig. 5a-b, the introduction of BPA and SMZ can enhance the reduction of Cr (VI). Interestingly, from Fig. 5c, another finding is that the higher the degradation rate of pollutants is, the more conducive to the synergistic reduction of Cr (VI). This phenomenon may be attributed to the difference in the electron-donating ability of different pollutant molecules in the BPA or SMZ/g-C<sub>3</sub>N<sub>4</sub> system, i.e., the difference in the ability to lose electrons. Based on previous studies, ionization potential (IP) is a good indicator to evaluate the ability of molecules to lose electrons [60–62]. It is defined as the energy needed to lose an electron from a neutral state A and become a positive ion A<sup>+</sup>, as shown in the formula (1).

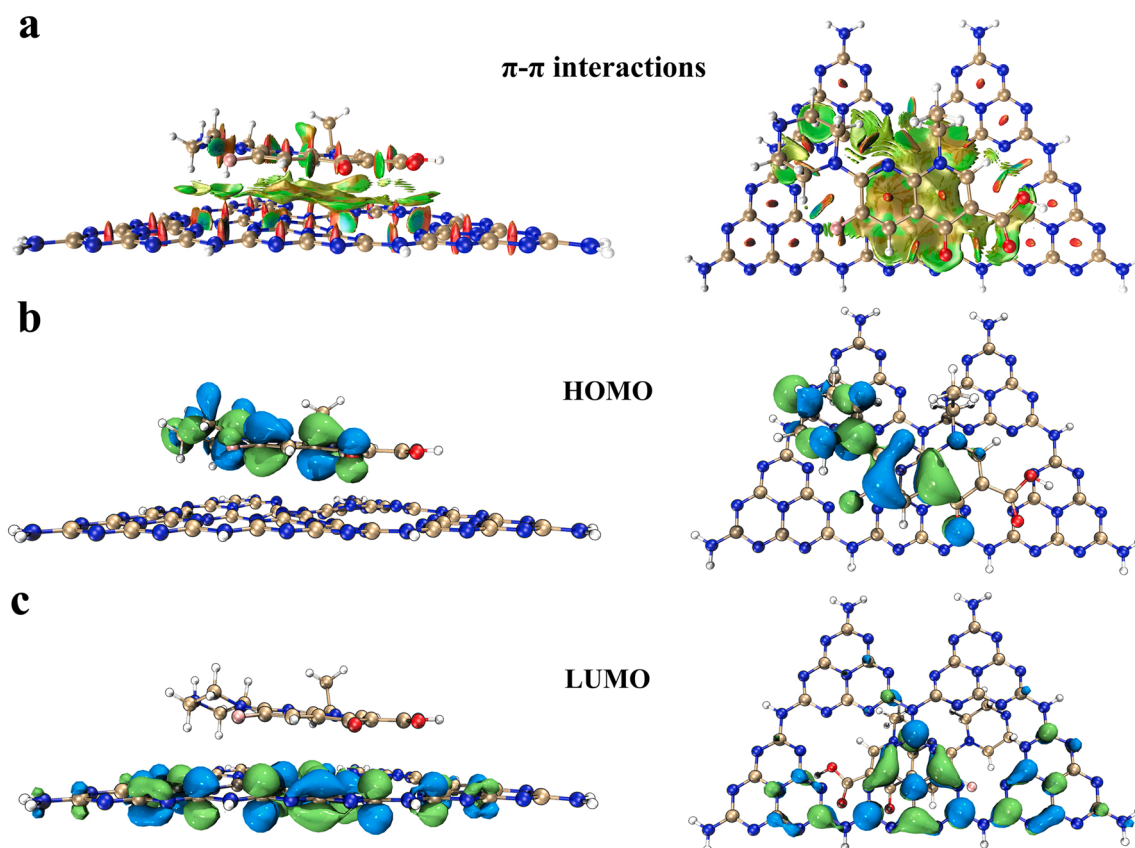


**Fig. 4.** (a) The  $\pi$ - $\pi$  interactions between ENO and g-C<sub>3</sub>N<sub>4</sub>. (b) The distribution of HOMO and (c) LUMO in the ENO/g-C<sub>3</sub>N<sub>4</sub> system. (white, H; gold, C; blue, N; red, O; pink, F).

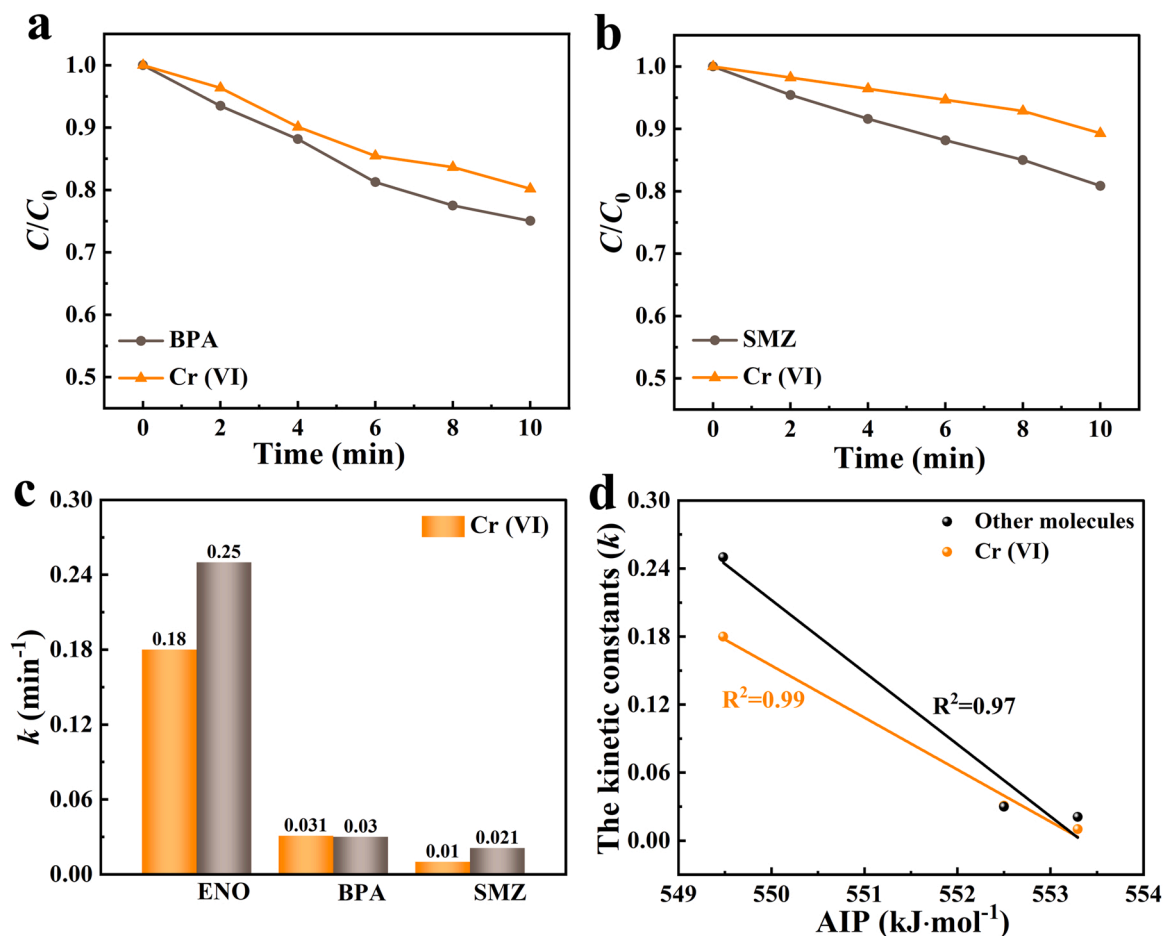


**Fig. 5.** The removal of (a) BPA and Cr (VI) (b) SMZ and Cr (VI) in the coexistence system. (c) The corresponding first-order reaction kinetic constants of ENO, BPA, SMZ and Cr (VI) by CNN. (d) The linear relationship between  $k$  and the AIP of ENO, BPA and SMZ. [ $M_{\text{ENO}} = M_{\text{BPA}} = M_{\text{SMZ}} = 0.0625 \text{ mmol L}^{-1}$ ].

$$\text{IP} = E(\text{N-1}) - E(\text{N}) \quad (1)$$

$N$  represents the number of electrons at electrically neutral [62]. Here, adiabatic IP (AIP) is obtained by optimizing the molecular structures of the N-1 and N systems respectively and then calculating the energy difference between them. The energy difference should be calculated in terms of the enthalpy ( $H$ ) of N-1 and N systems according to formula (2). Noteworthy, Solvation Model Based on Density (SMD) has been used in the theoretical calculation.

$$\text{AIP} = H(\text{N-1}) - H(\text{N}) + H(e) \quad (2)$$

Where  $H(\text{N-1})$  and  $H(\text{N})$  represent the enthalpy of optimized N-1 and N systems.  $H(e)$  is the enthalpy of single electron, which can be ignored owing to its small order of magnitude [60]. Hence, the AIP of ENO, BPA and SMZ is calculated to be 549.48, 552.50 and 553.29  $\text{kJ mol}^{-1}$ , respectively. Theoretically, the smaller AIP value is, the more likely the molecule is to lose electrons during the reaction. Thus, the ability to lose electrons or electron-donating of ENO is stronger than that of BPA and SMZ. Further, a linear relationship with  $R^2 = 0.99$  is found between the AIP of pollutant molecules and the  $k$  of Cr (VI) (Fig. 5d). Another linear relationship with  $R^2 = 0.97$  is also built between the AIP of pollutant molecules and the  $k$  of other molecules (ENO, BPA and SMZ). It demonstrates that pollutant molecules as electron donors can obviously improve the synergistic reduction of Cr (VI). Moreover, the pollutant molecules with higher electron-donating ability are more favorable to the increase of synergistic efficiency.

The effect of the concentration of ENO on the reduction efficiency of Cr (VI) is also investigated. As inspected in Fig. 6a, the removal rate of Cr

(VI) improved from 38.1% to 81.1% along with the concentration of ENO raised from 5  $\text{mg L}^{-1}$  to 20  $\text{mg L}^{-1}$  and the corresponding  $k$  are 0.06  $\text{min}^{-1}$ , 0.13  $\text{min}^{-1}$ , 0.15  $\text{min}^{-1}$  and 0.17  $\text{min}^{-1}$ , respectively (Fig. 6b). It is attributed to that the higher concentration of ENO would consume more  $\text{h}^+$  on the surface of g- $\text{C}_3\text{N}_4$ , which is conducive to Cr (VI) to obtain more  $\text{e}^-$ . However, the degradation efficiency of ENO decreases with the increase of ENO concentration (Fig. 6c). From Fig. 6d, the corresponding  $k$  are 0.57  $\text{min}^{-1}$ , 0.47  $\text{min}^{-1}$ , 0.32  $\text{min}^{-1}$  and 0.26  $\text{min}^{-1}$ , respectively. It is due to the adsorption and active sites on the surface of catalysts are limited, and a lower concentration of ENO would result in a higher adsorption rate, which can facilitate the degradation of ENO (Fig. S12). Overall, the higher concentration of ENO as electron donors is favorable to the synergistic reduction of Cr (VI). It should be noted that the reduction of Cr (VI) may also be unfavorable when the concentration of ENO reaches a certain level owing to the competition between them for reaction sites.

The pH value of solution plays a crucial role in the photocatalytic process because it affects the forms of pollutants and the surface potential of the photocatalysts. Here, the changes of the synergistic effect are studied by varying the pH value of solution. As exhibited in Fig. 7a-b, the acidic condition (pH = 3.0, 5.0) is more conducive to the synergistic reduction of Cr (VI) whether in the single or coexistence systems, while the alkaline condition (pH = 9.0, 11.0) is unfavorable to the reduction efficiency of Cr (VI). Based on the species distribution of Cr (VI) under different pH conditions (Fig. 7c), it is obvious that the main form of Cr (VI) is  $\text{HCrO}_4^-$  in the acidic environment (pH < 7), while the dominant form of Cr (VI) is  $\text{CrO}_4^{2-}$  in the alkaline environment (pH > 7). In acidic conditions, the excess hydrogen ions ( $\text{H}^+$ ) are beneficial for the

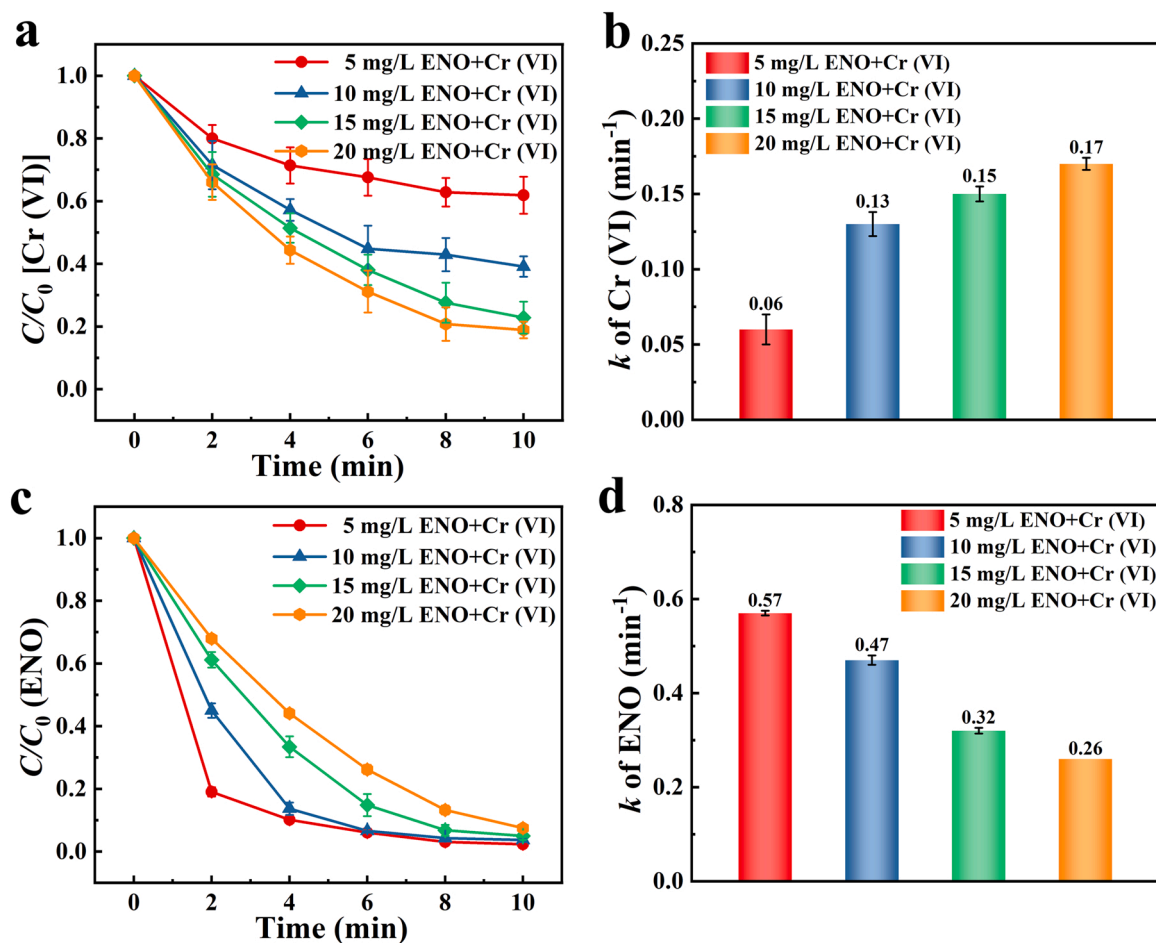
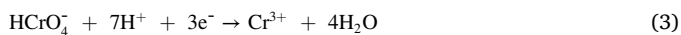


**Fig. 6.** The effect of ENO concentration on the (a) Cr (VI) reduction and (c) ENO degradation in the coexistence system. The corresponding first-order kinetic constants of (b) Cr (VI) and (d) ENO.

reduction of  $\text{HCrO}_4^-$  owing to the corresponding reaction process (formula (3)). However, in alkaline conditions, the abundant hydroxide ions ( $\text{OH}^-$ ) make the reduction of  $\text{CrO}_4^{2-}$  ions reduction process hard to proceed smoothly (formula (4)).



Besides, according to the analysis of zeta potential of CNN in different pH solution (Fig. S10), the surface of g- $\text{C}_3\text{N}_4$  displays a positive charge in acidic solution (pH = 3.0, 5.0), which provides a nice adsorption environment for  $\text{HCrO}_4^-$  ions. Whereas, the g- $\text{C}_3\text{N}_4$  with a more negative charge is not beneficial to the adsorption of  $\text{CrO}_4^{2-}$  in alkaline solution (pH = 9.0, 11.0) owing to the effect of electrostatic repulsion (Fig. S13a). Interestingly, the synergistic reduction of Cr (VI) in the coexistence system is promoted a lot under acidic conditions, in which Cr (VI) is completely removed within 4 min. This finding provides us with an idea to explore ways to enhance the removal efficiency of pollutants. Uncommonly, the degradation rate of ENO is suppressed in acidic (pH = 3.0, 5.0) and alkaline (pH = 9.0, 11.0) solution, as displayed in Figs. 7d and 7e. This phenomenon is worthy of further survey. Based on previous research, there are three forms of ENO due to two ionizable functional groups including the 3-carboxyl group and the N of piperazine substituent (Fig. S14). The detailed ionization process and species distribution of ENO are exhibited in Fig. 7f. Apparently, the main form of ENO in acidic, neutral and alkaline solutions is  $\text{ENO}^+$ ,  $\text{ENO}^0$  and  $\text{ENO}^-$ , respectively. ENO exists as an intermediate zwitterion ( $\text{ENO}^0$ ) in neutral solution (pH = 6.5), which can be adsorbed and degraded very

well owing to the surface potential of CNN being negative (−18.3 mV). Differently, the surface of CNN and ENO will carry the same charge in acidic (pH = 3.0, 5.0) or alkaline (pH = 9.0, 11.0) solutions, which hampered the adsorption process of ENO (Fig. S13b). Accordingly, the best degradation efficiency of ENO is achieved under neutral solution (pH = 6.5) both in single and the coexistence system. Overall, these results shown that the synergistic reduction efficiency of Cr (VI) would be remarkably improved in the acidic condition. While, the neutral condition is more favorable to the synergistic degradation of ENO.

### 3.5. The degradation mechanism of ENO

To further investigate the degradation of ENO by CNN in the coexistence system, three-dimensional (3D) EMMs experiment is carried out. As depicted in Fig. 8, the emission (Em) peak of ENO is located at 350–450 nm and the excitation (Ex) peak is located at 250–350 nm. From Fig. 8a–c, the peak intensity gradually increases, indicating that intermediate products are produced during the degradation process of ENO and the concentration of intermediate products is rising. Subsequently, the peak intensity gradually decreases, which demonstrates that the produced intermediate products are degraded, as shown in Fig. 8d–f. The above experimental result implies that CNN has a good degradation effect on ENO in the coexistence system.

In order to better understand the structural changes of ENO in the degradation process, the theoretical calculation based on DFT is employed to predict the reactive sites of the ENO molecule. As displayed in Fig. 9a, the structure of ENO contains piperazinyl, naphthyridine carboxyl and F atom. In general, the HOMO and LUMO of the molecule



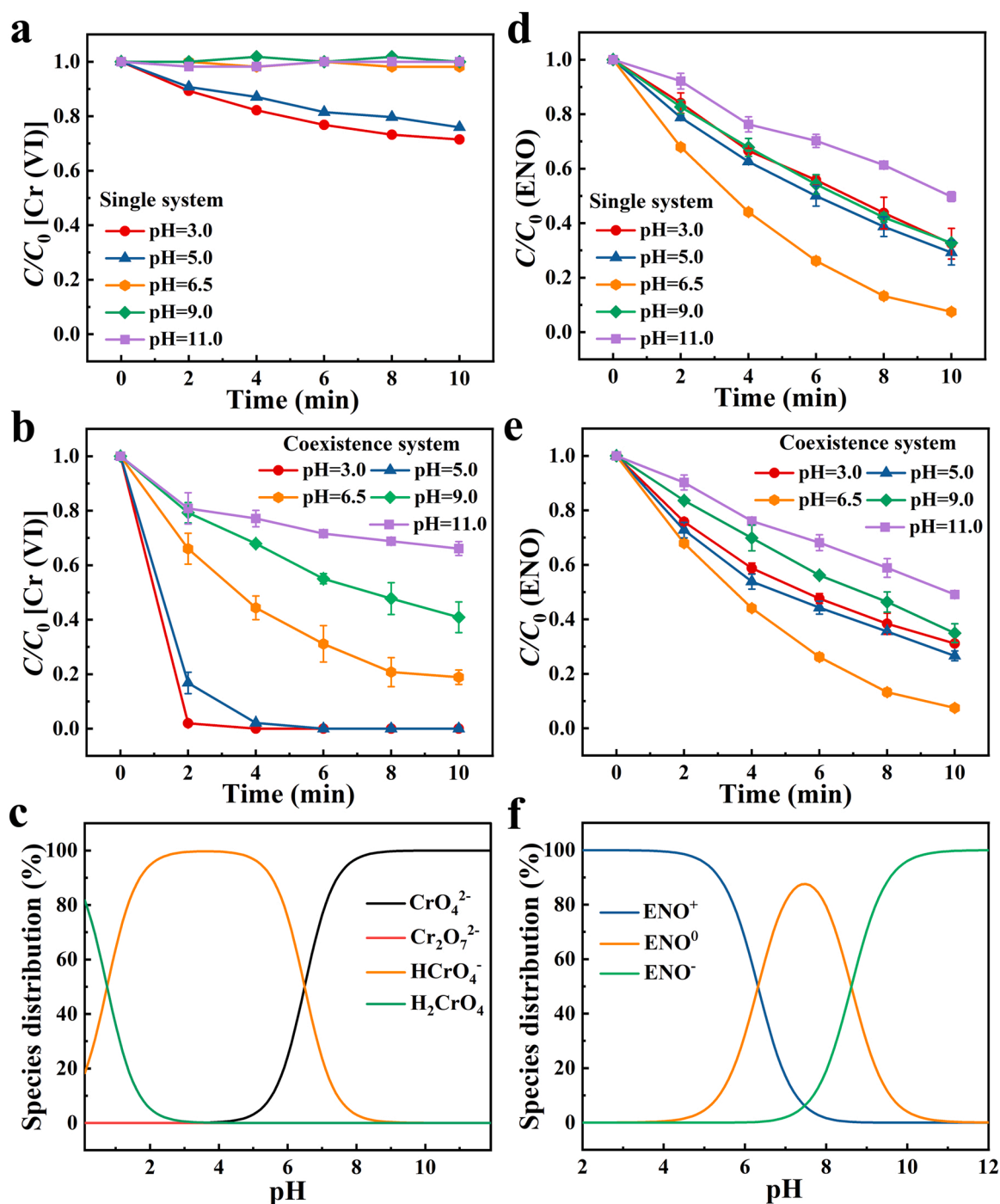


**Fig. 7.** The influence of pH value on the reduction of Cr (VI) in the (a) single and (b) coexistence system. (c) The existence forms of Cr (VI) in different pH solution. The influence of pH value on the ENO degradation in the (d) single and (e) coexistence system. (f) The existence forms of Cr (VI) in different pH solution. [ $C_{\text{ENO}} = 20 \text{ mg L}^{-1}$ ,  $C_{\text{Cr(VI)}} = 2 \text{ mg L}^{-1}$ ].

usually represent the ability to be oxidized or reduced. From Fig. 9b-c, it is clear that the HOMO of ENO is located in the piperazine ring, C3 and C5 atoms, while the LUMO of ENO is mainly concentrated in the two pyridine rings except for C2 and C3 atoms. The electrostatic potential spectrum (EPS) of the ENO molecule is exhibited in Fig. 9d, the blue area is the electron-rich region, which could be easily attacked by electrophilic reagents ( $\text{h}^+$ ,  $\cdot\text{OH}$ ). The red area is the electron-poor region, which is inclined to be attacked by nucleophilic reagents ( $\cdot\text{O}_2$ ). The white area is zero MEP region. Based on the above analysis, it is initially determined that the reaction sites of ENO are mainly concentrated around the piperazine ring and the N region of the two pyridine rings.

The Fukui index is utilized to further predict the feasibility of free radical attack on ENO. Generally,  $f^+$  represents nucleophilicity, the sites with higher  $f^+$  value are susceptible to the attack by nucleophilic species ( $\cdot\text{O}_2$ ).  $f^-$  represents electrophilicity, the sites with a higher  $f^-$  value are conducive to the attack of electrophilic species ( $\text{h}^+$  and  $\cdot\text{OH}$ ).  $f^0$  represents the ability to react with free radicals, the sites with higher  $f^0$  value are vulnerable to the attack by  $\cdot\text{O}_2$  and  $\cdot\text{OH}$ . Moreover, condensed dual descriptor (CDD) is a comprehensive index of nucleophilicity and electrophilicity. The green area is nucleophilicity, corresponding to the positive value. The blue area is electrophilicity, corresponding to the negative value. The detailed calculation results about natural population

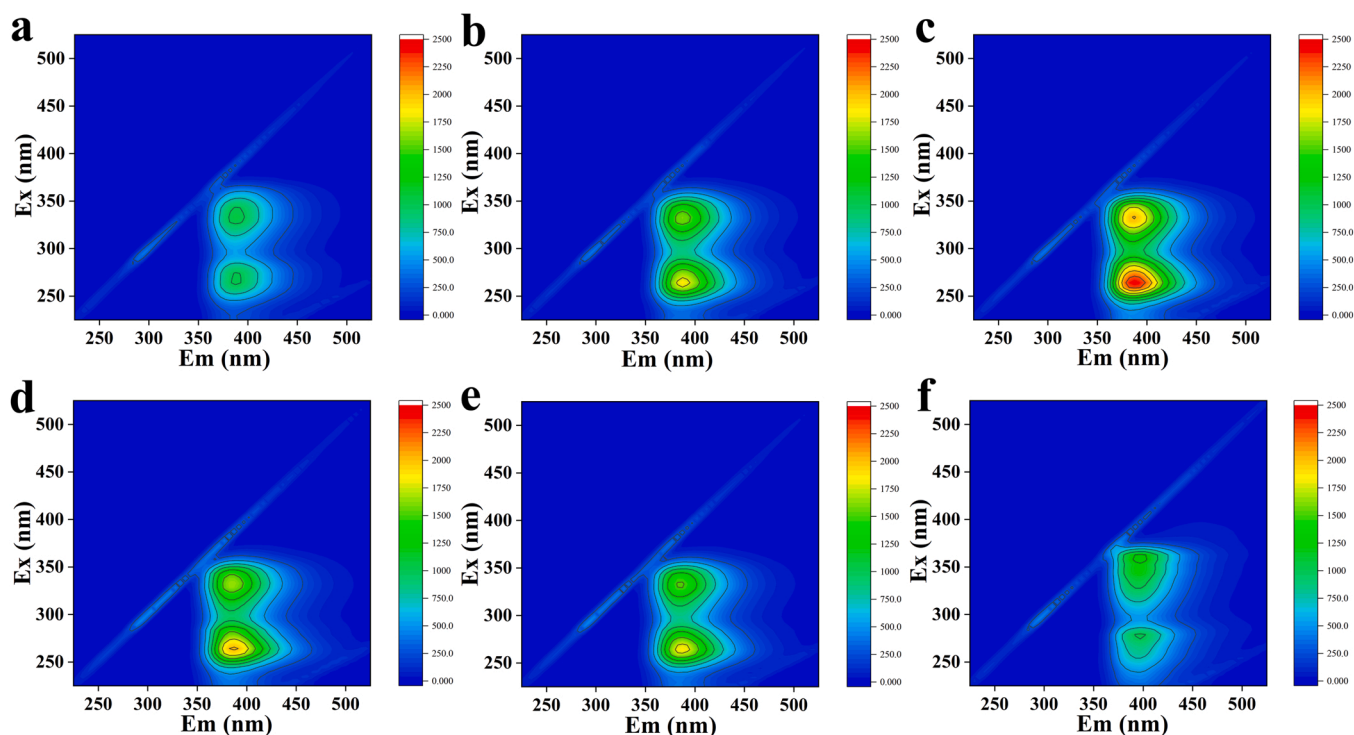


Fig. 8. 3D EEMs of ENO in the coexistence system: (a) take from the original solution; (b-f) collected after irradiation times of 2, 4, 6, 8 and 10 min, respectively.

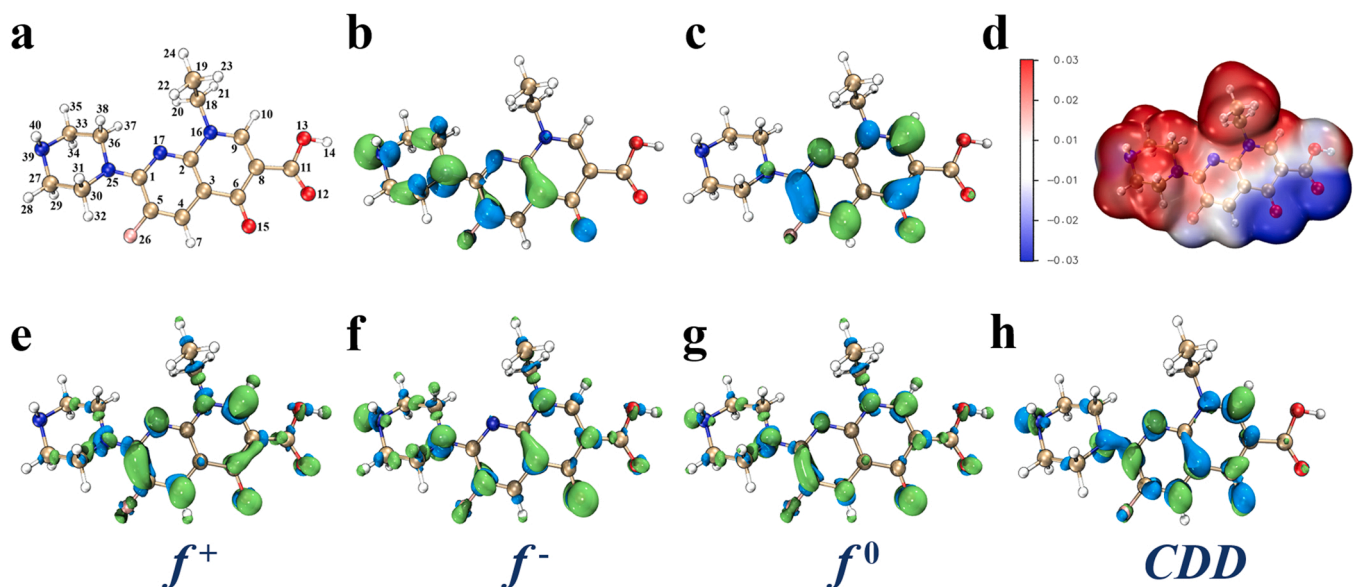


Fig. 9. (a) Chemical structure of ENO. (b) HOMO and (c) LUMO distributions on ENO. (d) ESP mapping of ENO. (e)  $f^+$ , (f)  $f^-$ , (g)  $f^0$  and (h) CDD distributions on ENO.

analysis (NPA) charges and Fukui index of ENO are depicted in Fig. S15. The isosurface images of the Fukui function distribution are displayed in Fig. 9e–h. obviously, C1, C4, C6, C9 and N17 exhibit significant nucleophilicity, while C2, C3, C8 and N16 show strong electrophilicity.

Based on the theoretical calculation of the ENO molecule, the attack sites of free radicals on ENO have been well researched. Combined with HPLC-MS determination, the feasible degradation pathways of ENO are proposed. 12 intermediates are verified and listed, and the feasible chemical structures are proposed according to HPLC-MS and previous studies (Table S1). As seen in Fig. 10, there are two pathways to the degradation of ENO. In pathway I, C4, C5 and C9 are easy to bind to  $\cdot\text{OH}$

due to their higher  $f^0$  value (0.0508, 0.0512 and 0.0586), and then C9 with the maximum CDD value (0.0715) is attacked by  $\text{h}^+$ , leading to the break of C8–C9 bond and the formation of D2 ( $m/z = 368$ ). After that, the removal reactions of carboxyl happen in C11 and N16, resulting in the production of D3 ( $m/z = 296$ ). The carboxyl in the C8 is further removed to form D5 ( $m/z = 254$ ). Ultimately, the piperazine ring is removed to produce D6 ( $m/z = 159$ ) owing to the higher CDD value of C1. In pathway II, N25 and N39 have lower CDD values ( $-0.0388$  and  $-0.0061$ ), which demonstrate that these two sites are prone to electrophilic reaction. Therefore, the N25 and N39 are broken to form D7 ( $m/z = 294$ ), and then N25 is continue broken to form D8 ( $m/z = 251$ ).

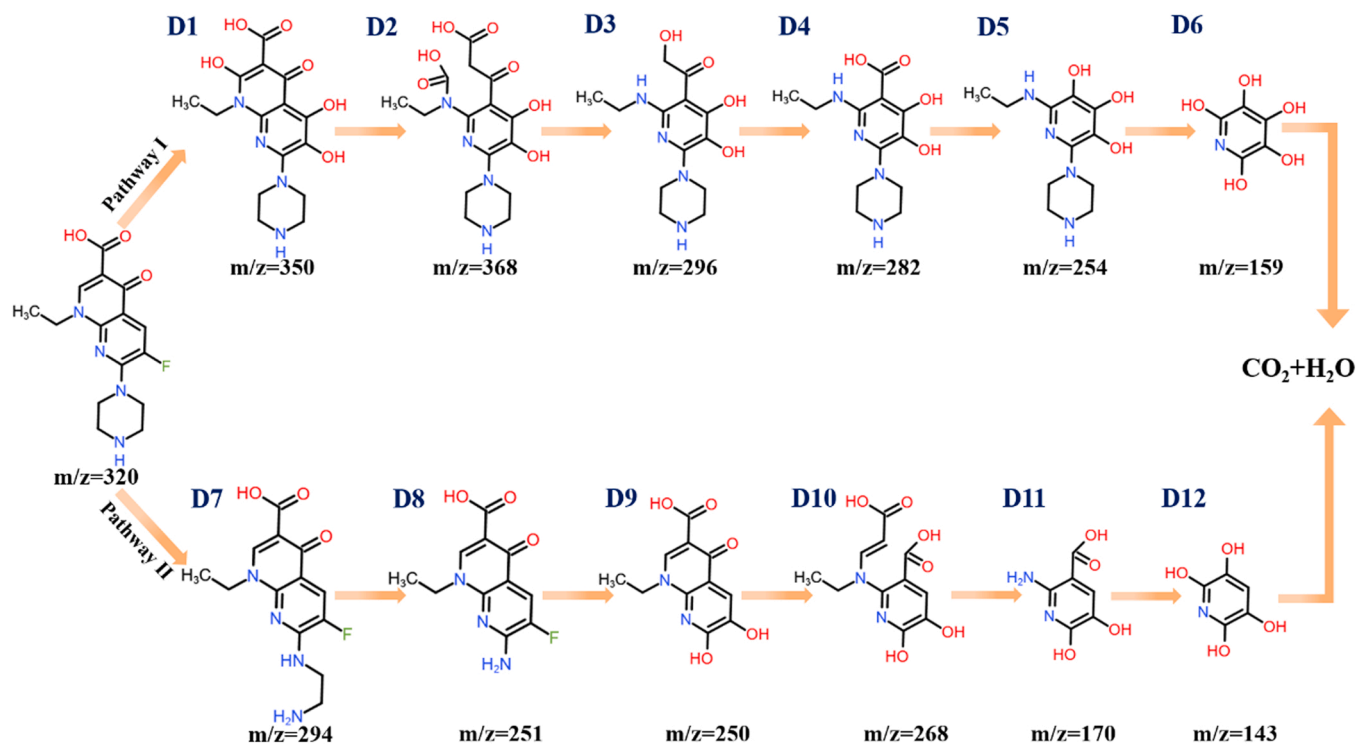


Fig. 10. The feasible degradation pathways for ENO degradation.

Afterward, amidogen and F atoms are replaced by hydroxyl owing to the higher  $f^0$  value, leading to the formation of D9 ( $m/z = 250$ ). Besides, the broken of C6-C8 and the removal of carboxyl occur in the subsequent degradation process. Finally, the production of D12 ( $m/z = 143$ ) is caused by the substitution of amino and carboxyl groups.

#### 4. Conclusion

In this work, the photocatalytic synergistic removal of ENO and Cr (VI) is achieved by CN and CNN. The experiments and DFT calculation demonstrate that ENO as electron donors can promote the separation of photo-generated carriers on g-C<sub>3</sub>N<sub>4</sub> and substantially improve the synergistic reduction efficiency of Cr (VI). Moreover, the decisive role of antibiotic molecules as electron donors on the synergistic effect is further proved through the study of the removal of the other two pollutants (BPA and SMZ) and Cr (VI). Another vital finding is that the electron-donating ability of contaminant molecule determines the synergistic removal efficiency, i.e., contaminant molecules with higher electron-donating ability are more favorable to the improvement of synergistic efficiency. After that, the effect of ENO concentration and pH value on the synergistic removal of ENO and Cr (VI) are surveyed. We find that the high concentration of ENO can promote the reduction of Cr (VI). Besides, the neutral solution is conducive to the degradation of ENO, while the acidic and alkaline solutions are not propitious to the degradation of ENO. For Cr (VI) ions, the reduction efficiency is high in acidic solutions and low in neutral and alkaline solutions. Subsequently, the degradation pathways of ENO are predicted by the theoretical calculation and HPLC-MS determination. Our work achieves the purpose of removing antibiotics and Cr (VI) synergistically in the coexistence system. The mechanism of synergistic effect is meaningful for the study of simultaneous elimination of contaminants in wastewater.

#### CRedit authorship contribution statement

**Qiang Zhang:** Methodology, Software, Validation, Visualization, Writing – original draft. **Juan Chen:** Data curation, Software,

Validation, Formal analysis, Writing – review & editing. **Xin Gao:** Calculation. **Huinan Che:** Validation, Writing – review & editing. **Pei-fang Wang:** Writing – review & editing, Data curation, Validation, Formal analysis. **Yanhui Ao:** Conceptualization, Writing – review & editing, Supervision, Funding acquisition, Data curation, Validation, Formal analysis.

#### Declaration of Competing Interest

The authors declare that they have no known competing financial interests or personal relationships that could have appeared to influence the work reported in this paper.

#### Acknowledgements

We are grateful for grants from National Natural Science Foundation of China (51979081, 52100179), Fundamental Research Funds for the Central Universities (B210202052), National Science Funds for Creative Research Groups of China (No. 51421006), and Priority Academic Program Development of Jiangsu Higher Education Institutions (PAPD).

#### Appendix A. Supporting information

Supplementary data associated with this article can be found in the online version at [doi:10.1016/j.apcatb.2022.121443](https://doi.org/10.1016/j.apcatb.2022.121443).

#### References

- [1] D. Wang, J. Chen, X. Gao, Y. Ao, P. Wang, Maximizing the utilization of photo-generated electrons and holes of g-C<sub>3</sub>N<sub>4</sub> photocatalyst for harmful algae inactivation, *Chem. Eng. J.* 431 (2022), 134105.
- [2] J. Zhang, Y. Li, X. Zhao, L. Wang, H. Chen, S. Wang, X. Xu, L. Shi, L. Zhang, Y. Zhu, Aligning potential differences within carbon nitride based photocatalysis for efficient solar energy harvesting, *Nano Energy* 89 (2021), 106357.
- [3] Z. Wang, X. Zheng, P. Chen, D. Li, Q. Zhang, H. Liu, J. Zhong, W. Lv, G. Liu, Synchronous construction of a porous intramolecular DA conjugated polymer via electron donors for superior photocatalytic decontamination, *J. Hazard. Mater.* 424 (2022), 127379.

- [4] J. Zhong, H. Jiang, Z. Wang, Z. Yu, L. Wang, J. Guo, Efficient photocatalytic destruction of recalcitrant micropollutants using graphitic carbon nitride under simulated sunlight irradiation, *Environ. Sci. Ecotechnol.* 5 (2021), 100079.
- [5] Z. Wu, X. Yuan, G. Zeng, L. Jiang, H. Zhong, Y. Xie, H. Wang, X. Chen, Highly efficient photocatalytic activity and mechanism of  $\text{Yb}^{3+}/\text{Tm}^{3+}$  codoped  $\text{In}_2\text{S}_3$  from ultraviolet to near infrared light towards chromium (VI) reduction and rhodamine B oxydative degradation, *Appl. Catal. B: Environ.* 225 (2018) 8–21.
- [6] Y. Zou, X. Wang, A. Khan, P. Wang, Y. Liu, A. Alsaedi, T. Hayat, X. Wang, Environmental remediation and application of nanoscale zero-valent iron and its composites for the removal of heavy metal ions: a review, *Environ. Sci. Technol.* 50 (2016) 7290–7304.
- [7] S. Murgolo, S. Franz, H. Arab, M. Bestetti, E. Falletta, G. Mascolo, Degradation of emerging organic pollutants in wastewater effluents by electrochemical photocatalysis on nanostructured  $\text{TiO}_2$  meshes, *Water Res.* 164 (2019), 114920.
- [8] H. Che, C. Liu, G. Che, G. Liao, H. Dong, C. Li, N. Song, C. Li, Facile construction of porous intramolecular g- $\text{C}_3\text{N}_4$ -based donor-acceptor conjugated copolymers as highly efficient photocatalysts for superior  $\text{H}_2$  evolution, *Nano Energy* 67 (2020), 104273.
- [9] A. Özcan, A. Özcan, Y. Demirci, E. Şener, Preparation of  $\text{Fe}_2\text{O}_3$  modified kaolin and application in heterogeneous electro-catalytic oxidation of enoxacin, *Appl. Catal. B: Environ.* 200 (2017) 361–371.
- [10] J. Hu, G. Chen, I. Lo, Removal and recovery of Cr(VI) from wastewater by maghemite nanoparticles, *Water Res.* 39 (2005) 4528–4536.
- [11] H. Li, F. Deng, Y. Zheng, H. Li, C. Qu, X. Luo, Visible-light-driven Z-scheme  $\text{rGO}/\text{Bi}_2\text{S}_3\text{-BiOBr}$  heterojunctions with tunable exposed BiOBr (102) facets for efficient synchronous photocatalytic degradation of 2-nitrophenol and Cr(VI) reduction, *Environ. Sci. Nano* 6 (2019) 3670–3683.
- [12] K. Li, J. Chen, Y. Ao, P. Wang, Preparation of a ternary g- $\text{C}_3\text{N}_4\text{-CdS}/\text{Bi}_4\text{O}_5\text{I}_2$  composite photocatalysts with two charge transfer pathways for efficient degradation of acetaminophen under visible light irradiation, *Sep. Purif. Technol.* 259 (2021), 118177.
- [13] Y. Guo, Y. Guo, D. Tang, Y. Liu, X. Wang, P. Li, G. Wang, Sol-gel synthesis of new  $\text{ZnFe}_2\text{O}_4/\text{Na-bentonite}$  composites for simultaneous oxidation of RhB and reduction of Cr(VI) under visible light irradiation, *J. Alloy. Compd.* 781 (2019) 1101–1109.
- [14] X. Gao, J. Chen, H. Che, Y. Ao, P. Wang, Rationally constructing of a novel composite photocatalyst with multi charge transfer channels for highly efficient sulfamethoxazole elimination: mechanism, degradation pathway and DFT calculation, *Chem. Eng. J.* 426 (2021), 131585.
- [15] J. Xu, J. Chen, Y.H. Ao, P.F. Wang, 0D/1D AgI/MoO<sub>3</sub> Z-scheme heterojunction photocatalyst: highly efficient visible-light-driven photocatalyst for sulfamethoxazole degradation, *Chin. Chem. Lett.* (2021) 3226–3230.
- [16] U. Aigbe, R. Das, W. Ho, V. Srinivasu, A. Maity, A novel method for removal of Cr (VI) using polypyrrole magnetic nanocomposite in the presence of unsteady magnetic fields, *Sep. Purif. Technol.* 194 (2018) 377–387.
- [17] J. Wang, T. Lin, G. Zeng, Y. Deng, C. Fei, 0D/2D interface engineering of carbon quantum dots modified  $\text{Bi}_2\text{WO}_6$  ultrathin nanosheets with enhanced photoactivity for full spectrum light utilization and mechanism insight, *Appl. Catal. B: Environ.* 222 (2018) 115–123.
- [18] J.F. Wang, J. Chen, P.F. Wang, J. Hou, C. Wang, Y.H. Ao, Robust photocatalytic hydrogen evolution over amorphous ruthenium phosphide quantum dots modified g- $\text{C}_3\text{N}_4$  nanosheet, *Appl. Catal. B: Environ.* 239 (2018) 578–585.
- [19] M. Nolan, A. Iwaszuk, A. Lucid, J. Carey, Design of novel visible light active photocatalyst materials: surface modified  $\text{TiO}_2$ , *Adv. Mater.* 28 (2016) 5425–5446.
- [20] A. Mukherji, R. Marschall, A. Tanksale, C. Sun, S. Smith, G. Lu, L. Wang, N-doped  $\text{CsTaWO}_6$  as a new photocatalyst for hydrogen production from water splitting under solar irradiation, *Adv. Funct. Mater.* 21 (2011) 126–132.
- [21] B. Lxna, B. Chda, B. Hqwa, L. Yan, B. Xlla, X. Chu, Preparation and characterization of  $\text{Fe}_2\text{O}_3/\text{Bi}_2\text{WO}_6$  composite and photocatalytic degradation mechanism of microcystin-LR-ScienceDirect, *Water Sci. Eng.* (2021) 109–118.
- [22] S. Zhou, Y. Wang, K. Zhou, D. Ba, Y. Ao, P. Wang, In-situ construction of Z-scheme g- $\text{C}_3\text{N}_4/\text{WO}_3$  composite with enhanced visible-light responsive performance for nitenpyram degradation, *Chin. Chem. Lett.* 32 (2021) 2179–2182.
- [23] J. Zhang, X. Chen, K. Takanabe, K. Maeda, K. Domen, J. Epping, X. Fu, M. Antonietti, X. Wang, Synthesis of a carbon nitride structure for visible-light catalysis by copolymerization, *Angew. Chem. Int. Ed.* 49 (2010) 441–444.
- [24] H. Kyung, J. Lee, W. Choi, Simultaneous and synergistic conversion of dyes and heavy metal ions in aqueous  $\text{TiO}_2$  suspensions under visible-light illumination, *Environ. Sci. Technol.* 39 (2005) 2376.
- [25] C. Chen, W. Ma, J. Zhao, Semiconductor-mediated photodegradation of pollutants under visible-light irradiation, *Chem. Soc. Rev.* 39 (2010) 4206–4219.
- [26] L. Xu, X. Bai, L. Guo, S. Yang, P. Jin, L. Yang, Facial fabrication of carbon quantum dots (CDs)-modified N-TiO<sub>2</sub>-x nanocomposite for the efficient photoreduction of Cr (VI) under visible light, *Chem. Eng. J.* 357 (2019) 473–486.
- [27] F. Chen, Q. Yang, Y. Wang, F. Yao, Y. Ma, X. Huang, X. Li, D. Wang, G. Zeng, H. Yu, Efficient construction of bismuth vanadate-based Z-scheme photocatalyst for simultaneous Cr(VI) reduction and ciprofloxacin oxidation under visible light: Kinetics, degradation pathways and mechanism, *Chem. Eng. J.* 348 (2018) 157–170.
- [28] Z. Huang, X. Dai, Z. Huang, T. Wang, L. Cui, J. Ye, P. Wu, Simultaneous and efficient photocatalytic reduction of Cr(VI) and oxidation of trace sulfamethoxazole under LED light by  $\text{rGO}/\text{Cu}_2\text{O}/\text{BiVO}_4$  p-n heterojunction composite, *Chemosphere* 221 (2019) 824–833.
- [29] K. Li, Z. Huang, S. Zhu, S. Luo, L. Yan, Y. Dai, Y. Guo, Y. Yang, Removal of Cr(VI) from water by a biochar-coupled g- $\text{C}_3\text{N}_4$  nanosheets composite and performance of a recycled photocatalyst in single and combined pollution systems, *Appl. Catal. B: Environ.* 243 (2019) 386–396.
- [30] Z. He, R. Liang, C. Zhou, G. Yan, L. Wu, Carbon quantum dots (CQDs)/noble metal co-decorated MIL-53(Fe) as difunctional photocatalysts for the simultaneous removal of Cr(VI) and dyes, *Sep. Purif. Technol.* 255 (2021), 117725.
- [31] M. Tang, Y. Ao, C. Wang, P. Wang, Rationally constructing of a novel dual Z-scheme composite photocatalyst with significantly enhanced performance for neonicotinoid degradation under visible light irradiation, *Appl. Catal. B: Environ.* 270 (2020), 118918.
- [32] I. Teixeira, E. Barbosa, S. Tsang, P. Camargo, Carbon nitrides and metal nanoparticles: from controlled synthesis to design principles for improved photocatalysis, *Chem. Soc. Rev.* 47 (2018) 7783–7817.
- [33] Y. Wu, J. Chen, H. Che, X. Gao, Y. Ao, P. Wang, Boosting  $2e^-$  oxygen reduction reaction in garland carbon nitride with carbon defects for high-efficient photocatalysis-self-Fenton degradation of 2, 4-dichlorophenol, *Appl. Catal. B: Environ.* 307 (2022), 121185.
- [34] M. Tang, Y. Ao, C. Wang, P. Wang, Facile synthesis of dual Z-scheme g- $\text{C}_3\text{N}_4/\text{Ag}_3\text{PO}_4/\text{AgI}$  composite photocatalysts with enhanced performance for the degradation of a typical neonicotinoid pesticide, *Appl. Catal. B: Environ.* 268 (2020), 118395.
- [35] H. Che, X. Gao, J. Chen, J. Hou, Y. Ao, P. Wang, Iodide-induced fragmentation of polymerized hydrophilic carbon nitride for high-performance quasi-homogeneous photocatalytic  $\text{H}_2\text{O}_2$  production, *Angew. Chem. Int. Ed.* 60 (2021) 25546–25550.
- [36] J. Xu, J. Song, P. Shi, Y. Min, Q. Xu, Mg-induced g- $\text{C}_3\text{N}_4$  synthesis of nitrogen-doped graphitic carbon for effective activation of peroxymonosulfate to degrade organic contaminants, *Chin. Chem. Lett.* (2021).
- [37] Q. Zhang, J. Chen, X. Gao, H. Che, Y. Ao, P. Wang, Understanding the mechanism of interfacial interaction enhancing photodegradation rate of pollutants at molecular level: Intermolecular  $\pi$ - $\pi$  interactions favor electrons delivery, *J. Hazard. Mater.* 430 (2022), 128386.
- [38] R. Mu, Y. Ao, T. Wu, C. Wang, P. Wang, Synthesis of novel ternary heterogeneous anatase- $\text{TiO}_2$  (B) biphasic nanowires/ $\text{Bi}_4\text{O}_5\text{I}_2$  composite photocatalysts for the highly efficient degradation of acetaminophen under visible light irradiation, *J. Hazard. Mater.* 382 (2020), 121083.
- [39] H. Frisch, G. Scuseria, M. Robb, J. Cheeseman, G. Scalmani, V. Barone, G. Petersson, H. Nakatsuji, X. Li, M. Caricato, A. Marenich, J. Bloino, B. Janesko, R. Gomperts, B. Mennucci, H. Hratchian, J. Ortiz, A. Izmaylov, J. Sonnenberg, D. Williams-Young, F. Ding, F. Lipparini, F. Egidi, J. Goings, B. Peng, A. Petrone, T. Henderson, D. Ranasinghe, V. Zakrzewski, J. Gao, N. Rega, G. Zheng, W. Liang, M. Hada, M. Ehara, K. Toyota, R. Fukuda, J. Hasegawa, M. Ishida, T. Nakajima, Y. Honda, O. Kitao, H. Nakai, T. Vreven, K. Throssell, J. Montgomery Jr., J. Peralta, F. Ogliaro, M. Bearpark, J. Heyd, E. Brothers, K. Kudin, V. Staroverov, T. Keith, R. Kobayashi, J. Normand, K. Raghavachari, A. Rendell, J. Burant, S. Iyengar, J. Tomasi, M. Cossi, J. Millam, M. Klene, C. Adamo, R. Cammi, J. Ochterski, R. Martin, K. Morokuma, O. Farkas, J. Foresman, D. J. Gaussian 16, Revision C.01, Fox, Gaussian, Inc, Wallingford CT, 2019.
- [40] P. Stephens, F. Devlin, C. Chabalowski, M. Frisch, Ab initio calculation of vibrational absorption and circular dichroism spectra using density functional force fields, *J. Phys. Chem. B* 98 (1994) 11623–11627.
- [41] P. Hariharan, J. Pople, The influence of polarization functions on molecular orbital hydrogenation energies, *Theor. Chim. Acta* 28 (1973) 213–222.
- [42] M. Frisch, J. Pople, J. Binkley, Self-consistent molecular orbital methods 25. Supplementary functions for Gaussian basis sets, *J. Chem. Phys.* 80 (1984) 3265–3269.
- [43] A. Marenich, C. Cramer, D. Truhlar, Universal solvation model based on solute electron density and on a continuum model of the solvent defined by the bulk dielectric constant and atomic surface tensions, *J. Phys. Chem. B* 113 (2009) 6378–6396.
- [44] T. Lu, F. Chen, Multiwfn: a multifunctional wavefunction analyzer, *J. Comput. Chem.* 33 (2012) 580–592.
- [45] S. Yang, Y. Gong, J. Zhang, L. Zhan, L. Ma, Z. Fang, R. Vajtai, X. Wang, P. Ajayan, Exfoliated graphitic carbon nitride nanosheets as efficient catalysts for hydrogen evolution under visible light, *Adv. Mater.* 25 (2013) 2452–2456.
- [46] M. Ding, J. Zhou, H. Yang, R. Cao, S. Zhang, M. Shao, X. Xu, Synthesis of Z-scheme g- $\text{C}_3\text{N}_4$  nanosheets/ $\text{Ag}_3\text{PO}_4$  photocatalysts with enhanced visible-light photocatalytic performance for the degradation of tetracycline and dye, *Chin. Chem. Lett.* 31 (2020) 71–76.
- [47] M. Groenewolt, M. Antonietti, Synthesis of g- $\text{C}_3\text{N}_4$  nanoparticles in mesoporous silica host matrices, *Adv. Mater.* 17 (2005) 1789–1792.
- [48] H. Che, L. Liu, G. Che, H. Dong, C. Liu, C. Li, Control of energy band, layer structure and vacancy defect of graphitic carbon nitride by intercalated hydrogen bond effect of  $\text{NO}_3^-$  toward improving photocatalytic performance, *Chem. Eng. J.* 357 (2019) 209–219.
- [49] B. Zhu, G. Jiang, S. Chen, F. Liu, Y. Wang, C. Zhao, Multifunctional Cl-S double-doped carbon nitride nanotube unit in catalytic ozone oxidation synergistic photocatalytic system: generation of ROS-rich region and effective treatment of organic wastewater, *Chem. Eng. J.* 430 (2022), 132843.
- [50] W. Niu, K. Marcus, L. Zhou, Z. Li, L. Shi, K. Liang, Y. Yang, Enhancing electron transfer and electrocatalytic activity on crystalline carbon-conjugated g- $\text{C}_3\text{N}_4$ , *ACS Catal.* 8 (2018) 1926–1931.
- [51] C. Hu, F. Chen, Y. Wang, N. Tian, T. Ma, Y. Zhang, H. Huang, Exceptional cocatalyst-free photo-enhanced piezocatalytic hydrogen evolution of carbon nitride nanosheets from strong in-plane polarization, *Adv. Mater.* 33 (2021), 2101751.



- [52] J. Di, J. Xia, X. Li, M. Ji, H. Xu, Z. Chen, H. Li, Constructing confined surface carbon defects in ultrathin graphitic carbon nitride for photocatalytic free radical manipulation, *Carbon* 107 (2016) 1–10.
- [53] Y. Ao, L. Xu, P. Wang, C. Wang, J. Hou, J. Qian, Preparation of CdS nanoparticle loaded flower-like Bi<sub>2</sub>O<sub>3</sub>CO<sub>3</sub> heterojunction photocatalysts with enhanced visible light photocatalytic activity, *Dalton Trans.* 44 (2015) 11321–11330.
- [54] X. Hu, W. Wang, G. Xie, H. Wang, X. Tan, Q. Jin, D. Zhou, Y. Zhao, Ternary assembly of g-C<sub>3</sub>N<sub>4</sub>/graphene oxide sheets/BiFeO<sub>3</sub> heterojunction with enhanced photoreduction of Cr(VI) under visible-light irradiation, *Chemosphere* 216 (2019) 733–741.
- [55] K. Wu, Z. Chen, H. Lv, H. Zhu, C.L. Hill, T. Lian, Hole removal rate limits photodriven H<sub>2</sub> generation efficiency in CdS-Pt and CdSe/CdS-Pt semiconductor nanorod-metal tip heterostructures, *J. Am. Chem. Soc.* 136 (2014) 7708–7716.
- [56] E. Johnson, S. Keinan, P. Mori-Sánchez, J. Contreras-García, A. Cohen, W. Yang, Revealing noncovalent interactions, *J. Am. Chem. Soc.* 132 (2010) 6498–6506.
- [57] S. Wang, X. Hai, X. Ding, S. Jin, Y. Xiang, P. Wang, B. Jiang, F. Ichihara, M. Oshikiri, X. Meng, Y. Li, W. Matsuda, J. Ma, S. Seki, X. Wang, H. Huang, Y. Wada, H. Chen, J. Ye, Intermolecular cascaded pi-conjugation channels for electron delivery powering CO<sub>2</sub> photoreduction, *Nat. Commun.* 11 (2020) 1149.
- [58] M. Fu, R. Shang, B. Zhao, B. Wang, Y. Fu, Photocatalytic decarboxylative alkylations mediated by triphenylphosphine and sodium iodide, *Science* 363 (2019) 1429–1434.
- [59] Y. Li, J.N. Evans, The Fukui function: a key concept linking frontier molecular orbital theory and the hard-soft-acid-base principle, *J. Am. Chem. Soc.* 117 (1995) 7756–7759.
- [60] J. Rimarčík, V. Lukeš, E. Klein, M. Ilčin, Study of the solvent effect on the enthalpies of homolytic and heterolytic N-H bond cleavage in p-phenylenediamine and tetracyano-p-phenylenediamine, *J. Mol. Struct.: Theochem.* 952 (2010) 25–30.
- [61] P. Nayak, N. Periasamy, Calculation of electron affinity, ionization potential, transport gap, optical band gap and exciton binding energy of organic solids using 'solvation' model and DFT, *Org. Electron.* 10 (2009) 1396–1400.
- [62] J. Li, Y. Wang, F. Wang, S. Liang, X. Lin, X. Chen, J. Zhou, A study on ionization potential and electron trap of vegetable insulating oil related to streamer inception and propagation, *Phys. Lett. A* 381 (2017) 3732–3738.